

NUMERICAL SIMULATION OF THE INTERACTION OF TWO CORONAL MASS EJECTIONS FROM SUN TO EARTH

N. LUGAZ, W. B. MANCHESTER IV, AND T. I. GOMBOSI

Center for Space Environment Modeling, University of Michigan, Ann Arbor, MI

Received 2005 April 26; accepted 2005 July 26

ABSTRACT

We present a three-dimensional compressible magnetohydrodynamics (MHD) model of the interaction of two coronal mass ejections (CMEs). Two identical CMEs are launched in the exact same direction into a preexisting solar wind, the second one 10 hr after the first one. Our global steady state coronal model possesses high-latitude coronal holes and a helmet streamer structure with a current sheet near the equator, reminiscent of near-solar minimum conditions. Within this model system, we drive the CMEs to erupt by the introduction of two three-dimensional magnetic flux ropes embedded in the helmet streamer. After an initial phase, when the trailing shock and the second CME propagate into the disturbed solar wind medium, they reach the edge of the first magnetic cloud, leading to complex magnetic interactions and a steep acceleration of the shock. Later, the trailing shock reaches the dense sheath of plasma associated with the leading shock, where it decelerates to a speed about 100 km s^{-1} larger than the speed of the leading shock. Eventually, the two shocks merge and a stronger, faster shock forms in association with a contact discontinuity between the “old” and “new” downstream regions. We find that the trailing shock always remains a fast-mode shock. A reverse shock is driven after the collision of the two magnetic clouds due to the difference in speed within the reconnection region. At Earth, the two magnetic clouds can still be distinguished, with a compressed and heated first cloud and a second overexpanded cloud. The transit time of this complex ejecta is reduced by about 6 hr compared to the case of the first CME without interaction. Our simulation is able to reproduce and explain some of the general features observed in satellite data for multiple magnetic clouds.

Subject headings: MHD — shock waves — Sun: coronal mass ejections (CMEs)

1. INTRODUCTION

Coronal mass ejections (CMEs), large-scale expulsions of plasma with a typical kinetic energy of 10^{31} – 10^{32} ergs, have been intensely studied in the last three decades. They range in speed from 30 to above 2700 km s^{-1} . The frequency of eruptions from the Sun depends strongly on the position in the 11 year solar cycle, from an average of 0.5 per day at solar minimum to 2–3 per day at solar maximum. One of the possible manifestations of CMEs at Earth is the passage of a magnetic cloud (MC), usually associated with an important geomagnetic activity. The characteristics of MCs, as defined by Burlaga et al. (1981), are an enhanced magnetic field, a smooth rotation of the magnetic field vector, and a low proton temperature. Recent studies have focused on the existence of more complex ejecta, with less defined characteristics and a possible association with interacting CMEs or a CME interacting with a corotating region (Burlaga et al. 2002), with the interaction of multiple MCs (Wang et al. 2002, 2003a), or with the effect of a shock overtaking a cloud (Wang et al. 2003b). According to Burlaga et al. (2002), only about one-third of Earth-directed solar eruptions leads to the passage of an MC at Earth; the majority of the ejections form either complex ejecta or multiple MCs (when the different MCs in the ejecta can still be distinguished at Earth).

Homologous eruptions provide a good example of potential interactions of CMEs on their way to Earth. Even though an active region rotates by about 3.5° in 6 hr (the smallest delay we found between two eruptions from the same active region), the large spatial scale of CMEs makes the interaction of successive homologous CMEs likely in this case. The eruptions on 1998 April 29–May 2 (AR 8210; SHINE campaign event),¹ 1998

November 4–5 (AR 8375), and 2000 September 15–16 (AR 9165; for the latter two events, see, e.g., Burlaga et al. 2002) are good examples of multiple Earth-directed eruptions from the same active region. A particularly interesting succession of eruptions occurred in 2000 November 24–27 (AR 9236), with six Earth-directed eruptions within 60 hr. In this particular case, the high frequency of eruptions is probably related to the high rate of magnetic flux emergence (Nitta & Hudson 2001).

It is also possible that eruptions from two adjacent active regions lead to the interaction of CMEs. This is probably the case for the eruptions on 2001 March 28–29, when the first eruption appears to originate from AR 9401 and a second eruption 11.4 hr later originating from AR 9393, leading to a multiple-MC event at Earth on 2001 April 30.

On the basis of two multiple-MC storms separated by two solar cycles, Farrugia & Berdichevsky (2004) present evolutionary signatures in complex ejecta. They find the following characteristics for both storms: heating of the plasma, acceleration (deceleration) of the leading (trailing) ejecta, compressed field and plasma in the leading ejecta, possible disappearance of shocks, and strengthening of the leading shock.

Another interesting phenomenon related to interacting CMEs is the acceleration of solar energetic particles (SEPs) by the fast MHD shock driven by CMEs (“gradual” events). Only 1%–2% of CMEs are found to be associated with SEPs. However, a high correlation is found between CME interaction in the lower heliosphere and SEP-rich events (Gopalswamy et al. 2002, 2003). Acceleration of SEPs by the front shock of a CME has been successfully simulated (Sokolov et al. 2004). Studying the generation of SEPs due to interacting CMEs requires first a better understanding of the physical processes underlying the shock-shock and shock-cloud interactions, as well as of the propagation of a CME into a disturbed medium.

¹ See <http://solarmuri.ssl.berkeley.edu/~welsch/public/SHINE/home.html>.

The propagation of a CME from the inner corona to 1 AU has been numerically modeled (e.g., Usmanov & Dryer 1995; Wu et al. 1999; Groth et al. 2000; Riley et al. 2002; Odstrcil et al. 2002; Manchester et al. 2004b) with increasing degrees of sophistication. There has not yet been a fully three-dimensional numerical simulation of the interaction of two or more CMEs from the Sun to the Earth. However, most of the different physical phenomena, which are likely to occur during the propagation of a second, faster CME overtaking a first, slower CME have been studied: the interaction of a shock wave with an MC (Vandas et al. 1997; Odstrcil et al. 2003), the interaction of two MCs (Odstrcil et al. 2003; Wang et al. 2005), and the acceleration of electrons associated with the shock-cloud interaction (Vandas & Odstrcil 2004)—all using 2.5-dimensional MHD numerical simulations—and the interaction of two shocks using one-dimensional hybrid numerical simulations (Cargill 1990) or a two-dimensional MHD simulation (Poedts et al. 2002).

We present here the results of a three-dimensional MHD simulation of the propagation and interaction of two identical CMEs from the Sun to the Earth. This approach has several advantages: first, we do not set one CME faster than the other. If the second CME overtakes the first one, it is, among other reasons, because of the reduced deceleration associated with its propagation in a less dense medium and the greater outward pressure gradient. Then it treats all the different possible interactions in a self-consistent fashion and at the same time. This approach provides moreover the first study of the propagation of a second CME in the solar wind disturbed by the passage of a first CME.

The simulation that this paper is based on is very similar to the one discussed in Manchester et al. (2004b). The steady state corona and bimodal solar wind are based on the model of Groth et al. (2000), which possesses open polar field lines and low-latitude closed field lines forming a streamer belt. Within this system, a first three-dimensional magnetic flux rope (taken from a family of analytical solutions of Gibson & Low [1998], hereafter GL98) is placed within the streamer belt with both ends tied to the inner boundary. The flux rope's properties are identical to those of the rope extensively studied in Manchester et al. (2004b). Thus, it gives us an “undisturbed” case to which we can compare our results, especially the arrival time of the CMEs at Earth. Ten hours later, an identical flux rope is placed at the same position within the streamer belt with the exact same parameters, and erupts again due to force imbalance. In addition to the study of the propagation of a single CME from Sun to Earth, this model has been used by Manchester et al. (2005) and Lugaz et al. (2005) to investigate the sheath and density structures of a CME.

The organization of the paper is as follows. We give a brief description of the conservative form of the equations of MHD and the scheme used to solve them in § 2. Details of the steady state corona and solar wind, as well as an outline of the GL98 flux rope model, are given in § 3. The evolution of the trailing shock as it propagates in the different media is described and analyzed in § 4. In § 5, the evolution of the two MCs is discussed. The generation of a reverse shock associated with the collision of the two MCs and with the reconnection between them is discussed in this section as well. The properties of the complex ejecta at Earth are described in § 6 followed by a comparison with real data from the *Advanced Composition Explorer (ACE)*. Finally, in § 7, we discuss the simulation results and the future work needed to get a more accurate picture of the interaction of two or more CMEs.

2. GOVERNING EQUATIONS OF THE MHD MODEL

In our model of the corona and heliosphere, we assume that the systems are composed of magnetized plasmas that behave

as an ideal gas with a polytropic index, $\gamma = 5/3$. The plasma is assumed to have infinite electrical conductivity so that the magnetic field is “frozen” into the plasma. Gravitational forces on the plasma are included, but only forces due to the Sun; there is no self-gravitation of the plasma. Finally, volumetric heating of the plasma of a chosen form is assumed to occur in the corona. With these assumptions, the evolution of the system may be modeled by the ideal MHD equations written in conservative form:

$$\frac{\partial \rho}{\partial t} + \nabla \cdot (\rho \mathbf{u}) = 0, \quad (1)$$

$$\frac{\partial(\rho \mathbf{u})}{\partial t} + \nabla \cdot \left[\rho \mathbf{u} \mathbf{u} + \left(p + \frac{B^2}{8\pi} \right) \mathbf{I} - \frac{\mathbf{B}\mathbf{B}}{4\pi} \right] = \rho \mathbf{g}, \quad (2)$$

$$\frac{\partial \mathbf{B}}{\partial t} + \nabla \cdot (\mathbf{u} \mathbf{B} - \mathbf{B} \mathbf{u}) = 0, \quad (3)$$

$$\begin{aligned} \frac{\partial \epsilon}{\partial t} + \nabla \cdot \left[\mathbf{u} \left(\epsilon + p + \frac{B^2}{8\pi} \right) - \frac{(\mathbf{u} \cdot \mathbf{B}) \mathbf{B}}{4\pi} \right] \\ = \rho \mathbf{g} \cdot \mathbf{u} + (\gamma - 1) Q, \end{aligned} \quad (4)$$

where ρ is the plasma mass density, \mathbf{u} the plasma velocity, \mathbf{B} the magnetic field, and p the plasma pressure (sum of the electron and ion pressures). The volumetric heating term, Q , parameterizes the effects of coronal heating, as well as heat conduction and radiation transfer (see § 3). The gravitational acceleration is defined as $\mathbf{g} = -g(\mathbf{r}/r)(R_\odot/r)^2$, where R_\odot is the solar radius and g is the gravitational acceleration at the solar surface. The total energy density, ϵ , is given by

$$\epsilon = \frac{\rho u^2}{2} + \frac{p}{\gamma - 1} + \frac{B^2}{8\pi}, \quad (5)$$

where gravity is omitted from the total since it is treated as a momentum source term. This system of eight equations describes the transport of mass, momentum, and energy with three equations describing the evolution of the magnetic field given by Faraday's law assuming infinite electrical conductivity. These equations are then put in dimensionless form, using values of the density and ion-acoustic wave speed from a suitable part of the physical domain (in this case the low corona) in addition to a reference length scale (in this case the solar radius). The dimensionless equations are then solved, using the block-adaptive tree solar wind Roe-type upwind scheme (BATS-R-US) code (Powell et al. 1999; Groth et al. 2000). This code is designed to run efficiently on massively parallel computers and solves the equations of MHD with the use of block adaptive mesh refinement (AMR). This feature of the grid allows for order-of-magnitude variation in numerical resolution within the computational domain. Such an adaptive grid is necessary to clearly resolve structures such as shocks and current sheets in the context of a global interacting coronal model extending beyond 1 AU.

3. MODELS OF THE SOLAR WIND AND OF THE CMEs

In order to simulate the time-dependent behavior of a CME propagating from the low corona through the solar wind, a representative MHD model of the steady state background solar wind is required. With such a model, the evolution of a CME is then formulated as a propagation problem with the initial condition of the corona and solar wind specified by the steady state solution.

In this section, we describe our steady state model of the corona and solar wind that is designed to approximately reproduce

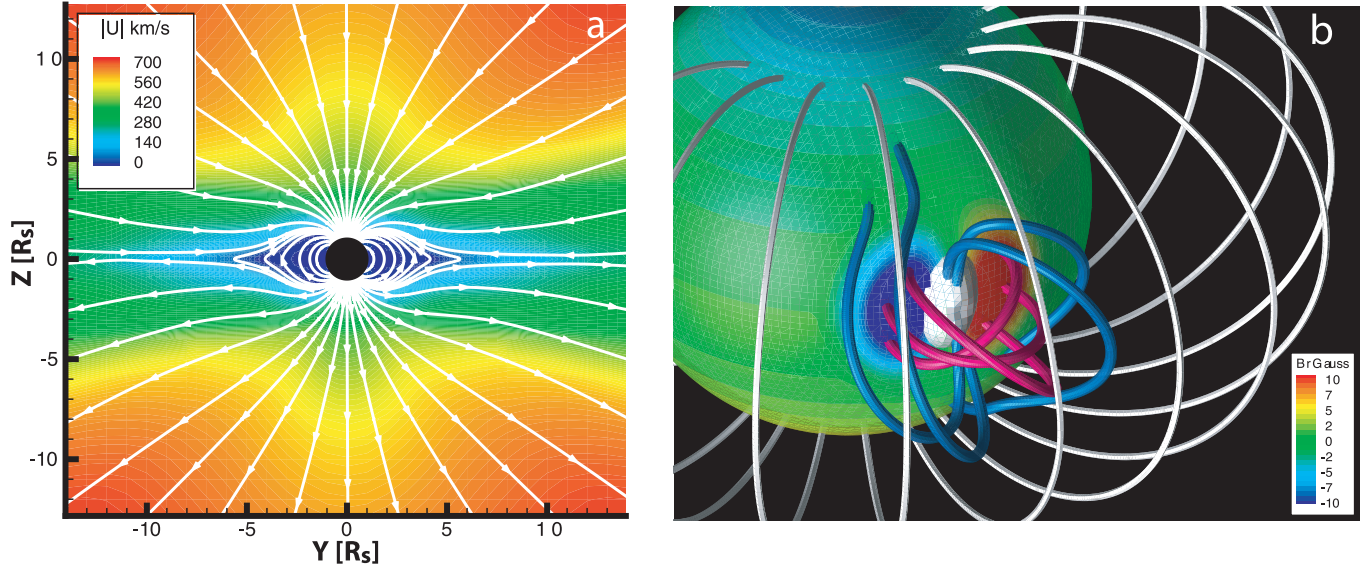


FIG. 1.—(a) Color image of the velocity magnitude of the steady state solar wind solution in the meridional y - z plane. “Streamlines” drawn in white illustrate the direction of the magnetic field in the plane. Note the bimodal nature of the solar wind speed. (b) Three-dimensional representation of the coronal magnetic field at $t = 0$ hr drawn as solid lines. The flux rope is drawn with magenta and blue lines showing, respectively, the toroidal and poloidal fields. The white surface is a density isosurface corresponding to 2×10^{16} g cm $^{-3}$ and showing the dense core contained in the GL98 flux rope. The false-color sphere shows the magnetic field strength at the surface of the Sun for our model.

conditions near solar minimum. The essential features of this model are (1) open magnetic field lines forming coronal holes at high latitude, (2) closed magnetic field lines forming a streamer belt near the Sun at low latitudes, and (3) the bimodal nature of the solar wind reproduced with fast wind over the poles and slow wind at low latitudes. A thin current sheet forms at the tip of the streamer belt and separates opposite-directed magnetic flux originating from the two poles. The model is simplified by alignment of the magnetic axis with the z -axis, so the solution is axisymmetric. Also, solar rotation is included since the domain extends to more than $300 R_\odot$, at which distance the azimuthal component of the Parker (1963) spiral is significant.

The corona is composed of high-temperature ($T > 10^6$ K), low-density ($\rho \approx 10^{-16}$ g cm $^{-3}$) plasma composed primarily of ionized hydrogen, which expands outward at supersonic speeds, and in doing so, forms the solar wind (Parker 1963). The steady state model of the corona and solar wind described here was first developed by Groth et al. (2000) and has since been modified as described in Manchester et al. (2004a, 2004b). The steady state numerical model is made with the assumption that the base of the corona is at the inner boundary and acts as a reservoir of hot plasma with an embedded magnetic field. The temperature of that plasma is taken to be 2.85×10^6 K with a plasma density of $\rho = 2.5 \times 10^{-16}$ g cm $^{-3}$. The intrinsic magnetic field at the solar surface, B_0 , may be written as a multipole expansion containing dipole and octupole moments. The dipole and octupole moments are chosen such that the maximum field strength is 8.4 G at the poles and 2.2 G at the equator. Volumetric heating of the model corona is introduced in a way that attempts to mimic the effects of energy absorption above the transition region, thermal conduction, and radiative losses, as well as satisfying known constraints of coronal heating. The heating scale height function is kept constant at $4.5 R_\odot$ in the streamer belt and increases inside the coronal hole, so that it varies from $4.5 R_\odot$ near the equator to $9 R_\odot$ at the poles. It is important to mention that this heating function was designed with several free parameters with the desire of reproducing observed overall features of the fast and slow solar wind.

Figure 1a depicts a two-dimensional cut through the three-dimensional steady state model showing a meridional slice. The false-color coding indicates the velocity magnitude, $|u|$, of the plasma, while the magnetic field is represented by solid white lines. The magnetic field remains closed at low latitude close to the Sun, forming a streamer belt. At high latitude, the magnetic field is carried out with the solar wind to achieve an open configuration. Closer to the equator, closed loops are drawn out and at a distance $r > 3 R_\odot$ collapse into a field reversal layer. The resulting field configuration has a neutral line and a current sheet originating at the tip of the streamer belt similar to the numerical solution originally obtained by Pneuman & Kopp (1971). Inspection of Figure 1a reveals a bimodal outflow pattern with slow wind leaving the Sun below 400 km s $^{-1}$ near the equator and high-speed wind above 750 km s $^{-1}$ found above 30° latitude.

3.1. Computational Mesh

The computational domain for the simulation extends from $-192 R_\odot < x < 192 R_\odot$, $-48 R_\odot < y < 336 R_\odot$, and $-192 R_\odot < z < 192 R_\odot$ with the Sun placed at the origin and with the magnetic axis aligned with the z -axis. The system is initially resolved with 22,772 self-similar $6 \times 6 \times 6$ blocks containing a total of 4.9 million cells. The blocks are distributed in size over eight levels of refinement with each subsequent level of refinement using cells half the size of the previous level (in each dimension). In this case, cells range in size from 1/32 to $4 R_\odot$ and are spatially positioned to highly resolve the central body and the flux rope, as well as the heliospheric current sheet. AMR criteria are chosen so that blocks close to a chosen radial line with large time variations in density are preferentially refined. In this way, the high-resolution mesh tracks the shock and sheath of the CMEs along a particular radial direction. Before the launch of the second CME, the system is resolved with 38,494 blocks corresponding to 9.3 million cells ranging in size from 1/32 to $8 R_\odot$. Resolution along both shocks is maintained at least to $1/16 R_\odot$ to a distance of more than $125 R_\odot$ from the Sun. The system is resolved with a maximum number of cells over 14.4 million. During particular times, such as the collision of the trailing shock with the first cloud

or the shock-shock interaction, the resolution at the trailing shock is maintained at $1/32 R_{\odot}$.

3.2. Boundary Conditions

We specify appropriate boundary conditions at the inner boundary (the spherical surface $r = R_{\odot}$) and the outer boundary (the outer surfaces of the rectangular domain) in the following way. Coronal boundary conditions are a function of heliospheric latitude. In the coronal holes poleward of $\theta_0 = 17.5^{\circ}$, the following values are prescribed in ghost cells inside $r = R_{\odot}$: $\rho = 2.5 \times 10^{-16} \text{ g cm}^{-3}$, $p = 5.89 \times 10^{-2} \text{ dynes cm}^{-2}$, $\mathbf{u} = 0$, and $\mathbf{B} = \mathbf{B}_0$. These values are then allowed to interact with the solution inside our physical domain through the $r = R_{\odot}$ boundary by solving the Riemann problem at the boundary. The boundary is treated as a discontinuity in which the inside values are the prescribed boundary values, and the outside values are taken from the adjacent active cell. These conditions set up a pressure gradient that drives plasma away from the Sun and permits plasma to pass through the boundary as the mass source for the solar wind. In the streamer belt equatorward of θ_0 , the following values are prescribed just inside $r = R_{\odot}$: $\partial\rho/\partial r = 0$, $\partial p/\partial r = 0$, $\mathbf{u} = -\mathbf{u}_{\text{out}}$, and $\mathbf{B} = \mathbf{B}_{\text{out}}$, where the subscript “out” refers to the values just outside $r = R_{\odot}$, which are computed by the flow solution scheme. These conditions strictly enforce a zero flow at the boundary in both the radial and tangential directions, with the exception of solar rotational flow. The boundary conditions also enforce continuity of the magnetic field across $r = R_{\odot}$. This provision allows the magnetic field of the flux rope (prescribed in the streamer belt) to pass through the interface where the footpoints are effectively “line tied” to the rotating surface. At the outer boundary of the domain, the flow is superfast. Thus, all waves are exiting the domain, and no information from outside the domain propagates into the domain.

3.3. Flux Rope of Gibson & Low

The CMEs are initiated within this coronal model by linearly superimposing a three-dimensional Gibson-Low magnetic flux rope (GL98) in the streamer belt in an initial state of force imbalance as is reported by Manchester et al. (2004a, 2004b). The density structure of the model possesses a dense helmet streamer containing a cavity embedded with a prominence-type density enhancement. Such long-lived coronal structures are often observed to give rise to CMEs (e.g., Hundhausen 1993). Figure 1b shows a three-dimensional representation of the first GL98 flux rope embedded in the solar magnetic field. The dense prominence material is represented by a white isosurface at the base of the rope. Since the magnetic field strength of the flux rope goes smoothly to zero at the solar surface, the continuity of the magnetic field at the solar surface is enforced. With our inclusion of the GL98 flux rope into a numerical, steady state model of the corona and solar wind, we can allow the GL98 flux rope to interact self-consistently with a realistic structured solar wind. To begin, we do not prescribe a flow field to the flux rope and surrounding corona, but rather the CME results from an initial force imbalance due to a removal of part of the plasma in the flux rope. More substantial force imbalance results from insufficient background coronal plasma pressure to offset the magnetic pressure of the flux rope. The GL98 equilibrium state requires a significant outward increasing plasma pressure to offset the magnetic pressure in the upper portion of the magnetic flux rope. The background corona is insufficient to provide this pressure, which leaves the flux rope with unbalanced magnetic forces, which drive the eruption. The second flux rope is inserted at the exact same

position as the first one in the inertial frame. Since solar rotation is included in our model, the second CME does not originate from the same place on the solar surface as the first CME, but it will propagate in the exact same direction as the first one.

4. EVOLUTION OF THE TRAILING SHOCK

4.1. Overview

We first present an overview of the main phases of the propagation of the trailing shock with the upstream conditions it encounters. The second eruption is initiated 10 hr after the launch of the first one, at which time the leading shock is at $43.9 R_{\odot}$ with a speed of about 625 km s^{-1} and the flux rope center is at $32.3 R_{\odot}$ with a speed of about 500 km s^{-1} . For the first 4 hr, the trailing shock propagates into the disturbed solar wind (phase 1). Between times $t = 13.75$ and 14 hr, the trailing shock reaches the edge of the first MC and experiences the transition from a pressure-dominated (high- β) plasma to a magnetic-dominated (low- β) plasma. The shock-cloud interaction (phase 2) lasts for about 8.6 hr, during the first 3 hr, the β upstream of the shock is less than 0.1. Once the shock exits the MC, it enters the dense sheath of plasma associated with the leading shock (phase 3). This region can be considered unmagnetized (high β), and it takes 12 hr for the trailing shock to pass through the sheath. Then for 2 hr, the two shocks cannot be distinguished, even with a resolution of $1/32 R_{\odot}$. At time $t = 35.6$ hr, a new shock forms and propagates ahead of the two MCs into the undisturbed solar wind (phase 4). Eventually, at time $t = 66$ hr, the shock reaches Earth. The first MC reaches it 7.5 hr later, the second MC 16.6 hr afterward. The summary of the upstream conditions encountered by the trailing shock is shown in Figure 2a, with the number density in a logarithmic scale as a dotted line, the Alfvénic speed as a solid line, and the sonic speed as a dashed line. In the next subsections, we track the shock speed and compression ratio and relate them to the upstream conditions and the shock Mach numbers in the moving frame. Figure 3b shows a time-height plot of the shocks and centers of the flux rope from times $t = 0$ to 35 hr. Figures 5 and 6 show a false-color representation of the number density and velocity magnitude at, respectively, the end of phase 1 ($t = 13.75$ hr), during phase 2 ($t = 19$ hr), at the beginning of phase 3 ($t = 23.5$ hr), and just after the end of phase 3 ($t = 37$ hr).

4.2. Phase 1: Propagation of the Trailing Shock in the Disturbed Solar Wind

Previous studies (e.g., Webb et al. 1996) show that the mass of a CME increases after the initiation phase. This mass increase is due to an accretion of the mass that travels with the shock and that is taken away from the ambient coronal mass. Thus, the propagation of a first CME into the ambient solar wind removes some of the background’s mass. Associated with the propagation of the CME, there is as well a disruption of the solar wind, especially of the background magnetic field. As a consequence, as a second CME erupts in the same direction shortly after a first CME, it does not propagate into the quiet bimodal solar wind, but into a disturbed medium, less dense and more magnetized. This can be seen in Figure 3a, where the solar wind conditions in the current sheet ahead of the CME are shown just before the launch of the first CME (red lines) and just before the launch of the second CME (black lines).

After the first 2 hr, when the fast-mode wave driven by the second ejection is not yet a shock, the speed of the trailing shock in the frame moving with the upstream plasma is obtained through

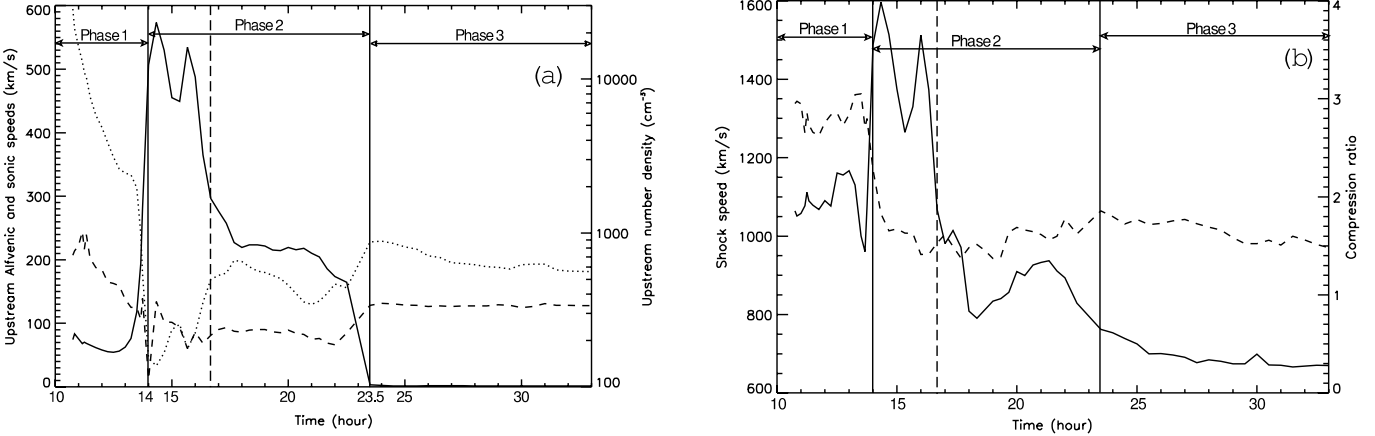


FIG. 2.—(a) Upstream conditions as observed just upstream of the trailing shock. *Solid line*: Alfvénic speed. *Dashed line*: Sonic speed. *Dotted line*: Number density in logarithmic scale. (b) Characteristics of the trailing shock. *Dashed line*: Compression ratio. *Solid line*: Speed in km s^{-1} . The second CME is initiated at time $t = 10$ hr. The two solid vertical lines in both panels correspond from left to right to the beginning and end of the shock-cloud interaction.

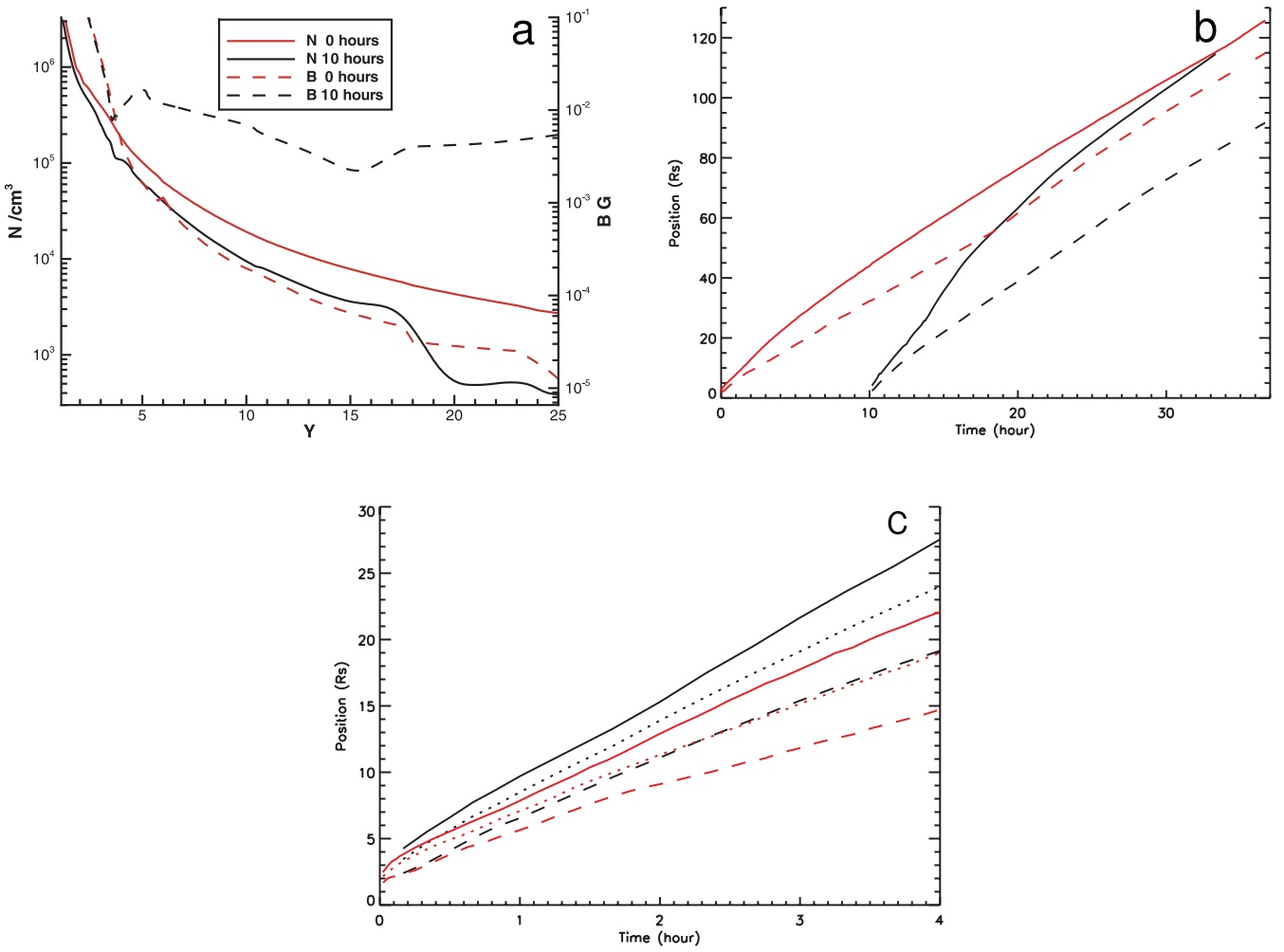


FIG. 3.—(a) Solar wind conditions in the current sheet before the launch of the two CMEs. *Solid lines*: Number density in a logarithmic scale. *Dashed lines*: Magnetic field in a logarithmic scale. *Red lines*: First CME, time $t = 0$ hr. *Black lines*: Second CME, time $t = 10$ hr. (b) Time-height plot of the shock (solid lines) and center of the flux rope (dashed lines). *Red lines*: First CME. *Black lines*: Second CME. (c) Comparison of the two shock waves (solid lines), flux rope top (dotted lines), and flux rope centers (dashed lines) as the two CMEs propagate in the solar wind before any interaction occurs. For the second CME, the time reference has been shifted by 10 hr, so that time $t = 0$ hr corresponds to the initiation of the second CME. *Red lines*: First CME. *Black lines*: Second CME.

the Rankine-Hugoniot relations, taking the speed and density at a position where the shock is normal:

$$V_{\text{shock}} = \frac{\rho_1 U_1 - \rho_0 U_0}{\rho_1 - \rho_0}, \quad (6)$$

where the subscripts 0 and 1 refer to the upstream and downstream conditions, respectively.

After a first phase of rapid acceleration, which lasts about 30 minutes, we find that the second shock wave is moving about $150\text{--}200 \text{ km s}^{-1}$ faster than the first shock wave at the same time. This phenomenon is expected, as it is a direct result of the first CME having removed some of the mass of the solar corona. Associated with this mass removal ahead of the second CME, the outward pressure gradient and fast-mode speed are greater for the second CME than for the first one. These combined effects lead to the trailing shock slowly overtaking the leading shock. Time-height plots of the two shock waves (and the associated CMEs) during the first 4 hr of their propagation in the solar corona can be seen in Figure 3c with the time reference of the second CME shifted by 10 hr to allow a direct comparison between the two CMEs.

4.3. Phase 2: Shock-Cloud Interaction

At time $t = 13$ hr, before reaching the rear edge of the first MC, the trailing shock is a fast-mode shock, propagating into a high- β medium ($\beta \sim 4$), with a speed of about 1150 km s^{-1} and a compression ratio of about 3. During the next hour, as the shock enters the first MC, the upstream β decreases by a factor of 100, the upstream density decreases by a factor of 15, the Alfvénic speed is multiplied by 8, and the sound speed remains quasi-unchanged (increase by a factor of 1.2). Moreover, the plasma upstream of the shock is locally sub-Alfvénic ($M_{A,\min} = 0.81$). Due to the reduced density encountered, the shock quickly accelerates to a maximum speed of 1572 km s^{-1} at time $t = 14.3$ hr. However, the high magnetic field of the region leads to a large reduction of the compression ratio of the shock, to a value of about 1.7. The shock remains fast ($V_{\text{shock}} \geq 1300 \text{ km s}^{-1}$) until it reaches the center of the cloud (denser), where it decelerates to a speed of about 850 km s^{-1} . The compression ratio remains low (less than 1.6) during the entire propagation of the shock in the cloud.

The trailing shock remains at all times a fast-mode shock, with a minimum Alfvénic Mach of 1.6 in the frame moving with the upstream plasma and always leads to an increase in the magnetic field strength. The shock speed and compression ratio for times up to 33 hr are plotted in Figure 2b, which can be analyzed with the help of the left panel of the same figure. The shock acceleration (deceleration) is found to be well correlated with the decrease (increase) in the upstream density. During its propagation in the MC, the shock proves to have a poor effectiveness at compressing the plasma. Similar results have been reported for a fast shock propagating into an MC (Odstrcil et al. 2003), concerning the shock acceleration and the decrease in amplitude of the shock, following in some cases, the propagation of a fast shock into an MC.

4.4. Phase 3: Shock Propagation into the Dense Sheath of Plasma

At time $t = 23.5$ hr, the trailing shock exits the MC and enters the dense sheath of plasma associated with the leading shock. The cloud and the sheath are separated by a contact discontinuity. This new region can be considered unmagnetized ($V_A \leq 3 \text{ km s}^{-1}$)

and thus highly plasma-dominated ($\beta \geq 2000$). The sound speed in this region is about 50% larger than in the MC ($c_s \sim 130 \text{ km s}^{-1}$) and the density twice as large. As the trailing shock enters this new region, its speed decreases from 850 to about 700 km s^{-1} , due to the increased upstream density. This speed is still about 120 km s^{-1} faster than the speed of the leading shock, so the trailing shock continues to overtake the leading shock, but with a slower rate. The difference in speed is low enough that it takes as much time for the trailing shock to overtake the last $8.8 R_\odot$ in the sheath as it took it to overtake the first $44.5 R_\odot$.

4.5. Shock-Shock Interaction

At time $t = 33.3$ hr, the two shock fronts are only $0.6 R_\odot$ apart, and from then until time $t = 35.7$ hr, it is not possible to distinguish between the two shocks, even with a resolution of $1/32 R_\odot$. However, we know that the structure resulting from the interaction of the two shocks is not a MHD shock yet, since it is associated with a density increase larger than 5, well above the theoretical limit of 4 for $\gamma = 5/3$. At time $t = 35.7$ hr, it is possible to distinguish a new fast-mode MHD shock. This new shock is stronger than the previous two shocks (1 hr average compression ratio of 3.59 compared to 1.52 and 3.13 for the trailing and leading shocks, respectively). It is also faster than the first shock by about 100 km s^{-1} and slower than the second shock by about 30 km s^{-1} . The plasma velocity in the “new” downstream region is almost identical to the plasma velocity in the “old” downstream region (the twice-shocked medium before the shocks’ merging). Since the total compression ratio of the two shocks before the merging was larger than 4, the “new” downstream region is, in effect, less dense than the “old” one. However, since the new shock is stronger than the previous two shocks, this “new” downstream region is also hotter (see Fig. 4). The different plasma conditions must be matched behind the shock by an MHD discontinuity (tangential or contact discontinuity) or a rarefaction wave. Since the overtaking shock was not pressure-driven, the pressure in the “old” downstream region is very rapidly decreasing. This decreasing pressure in the “old” downstream region and the reduced pressure in the “new” downstream region can be matched without any jump, simply by reducing the rate of the decrease in pressure in the “old” downstream region. Therefore, the pressure is continuous across the interface between the two downstream regions, and this interface is a contact discontinuity between the denser “old” downstream region and the hotter “new” downstream region.

5. EVOLUTION OF THE TWO MAGNETIC CLOUDS

5.1. Compression and Acceleration of the First Cloud by the Trailing Shock

The trailing shock enters the first MC around time $t = 13.6$ hr and passes the center of this cloud at time $t = 18.5$ hr. It leads to an acceleration of the cloud and a compression in the y -direction (see top panels of Figs. 5 and 6).

One of the ways to quantify the effects of the shock on the MC is to track the speed at the center of the first flux rope. We define the center of the flux rope as the point in the x - y plane along the $\{x = 0\}$ line, where B_z goes to zero. Until the shock reaches the center of the flux rope, the speed slowly decreases due to the expansion of the cloud. At the time the shock goes through the center of the flux rope, the speed increases by 110 km s^{-1} and continues to increase for the next five and a half hours, to reach a maximum speed of 660 km s^{-1} , 200 km s^{-1} faster than the speed at the center of the flux rope before the shock’s passage.

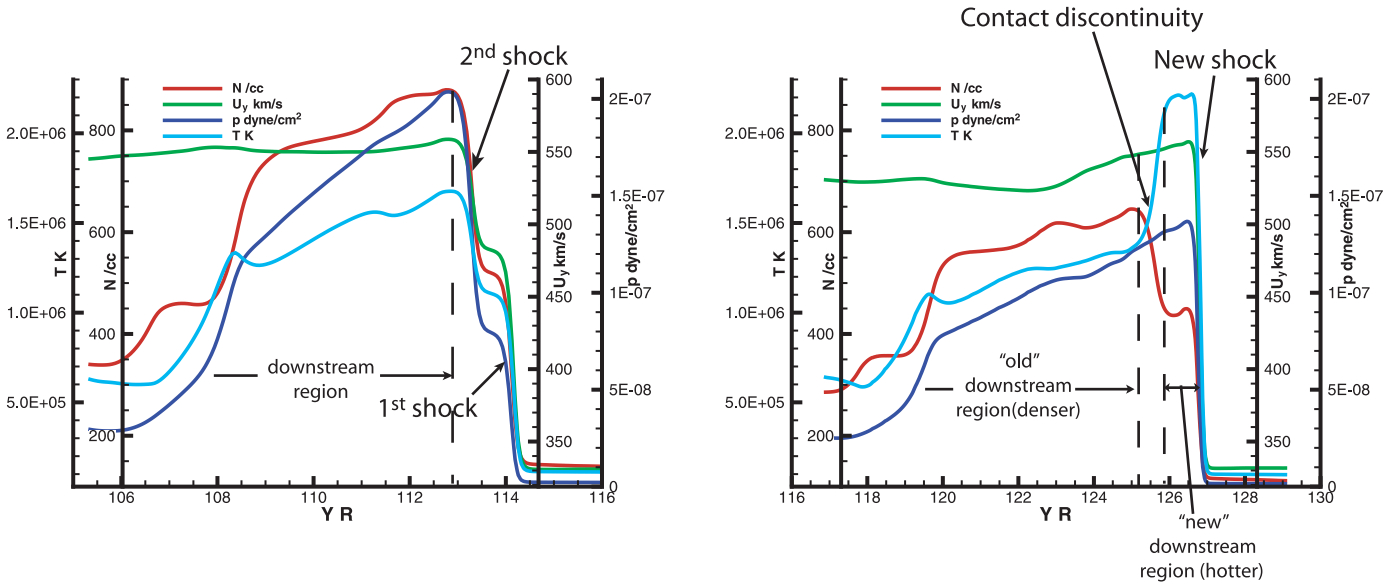


FIG. 4.—Plasma properties (number density in red, normal speed in green, thermal pressure in dark blue, and temperature in light blue) at time $t = 33$ hr (before the shocks' merging; *left*) and $t = 37$ hr (after the shock merging; *right*). The two panels have the same scale for the different plasma quantities. Note the larger temperature increase behind the shock after the shocks' merging, as well as the reduced rate of pressure decrease.

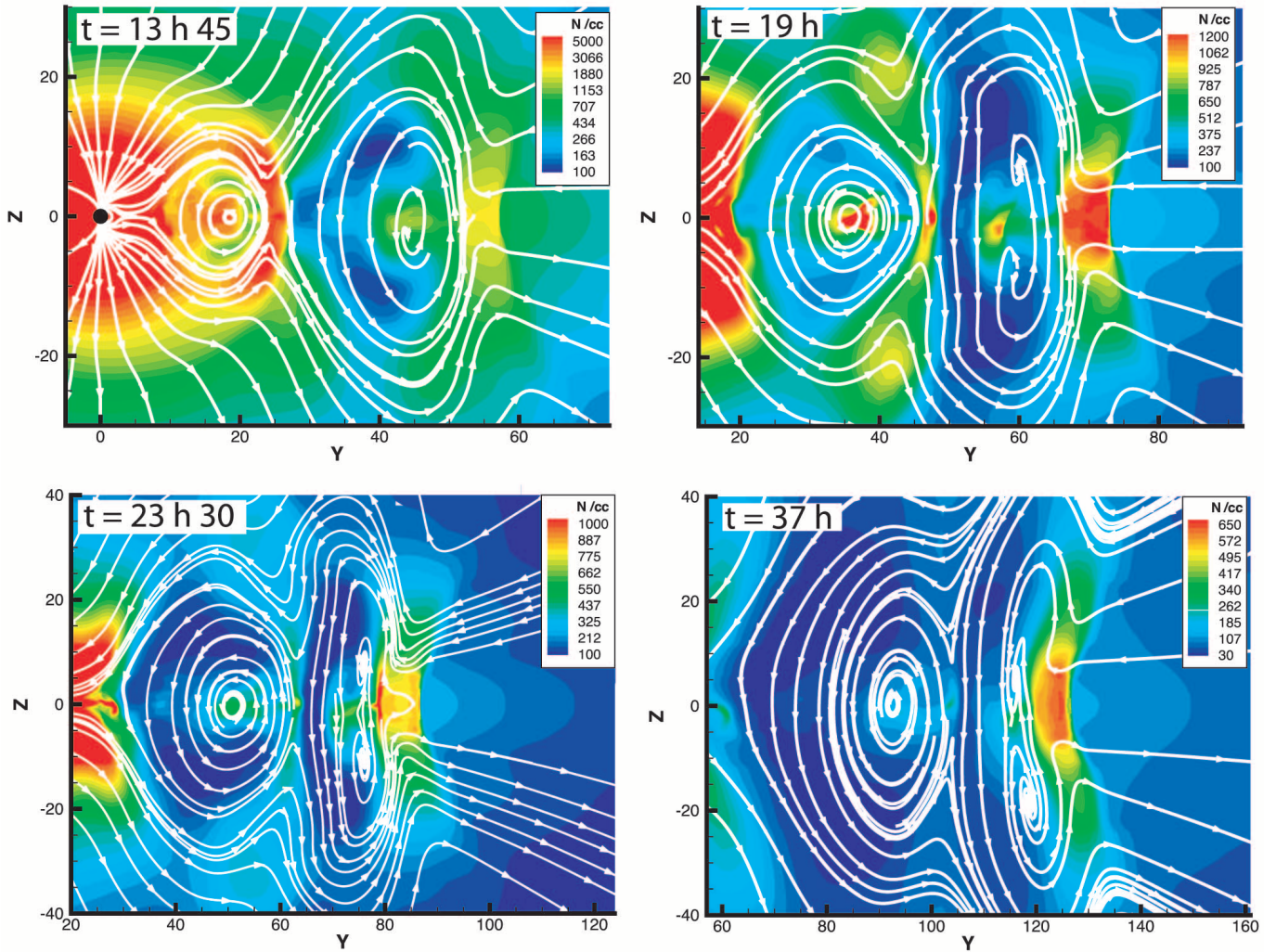


FIG. 5.—Number density in the y - z plane at four different times during the interaction of the two CMEs. ‘‘Streamlines’’ drawn in white illustrate the direction of the magnetic field in the plane. *Top left*: $t = 13.75$ hr, as the trailing shock enters the first cloud ($27.5 R_\odot$). *Top right*: $t = 19$ hr, as the trailing shock has just passed the center of the first cloud ($58.5 R_\odot$). *Bottom left*: $t = 23.5$ hr, as the trailing shock enters the dense sheath of plasma associated with the leading shock ($79.2 R_\odot$). *Bottom right*: $t = 37$ hr; a new shock has formed, followed by a contact discontinuity ($126.8 R_\odot$). Note the change in scales between the different panels.

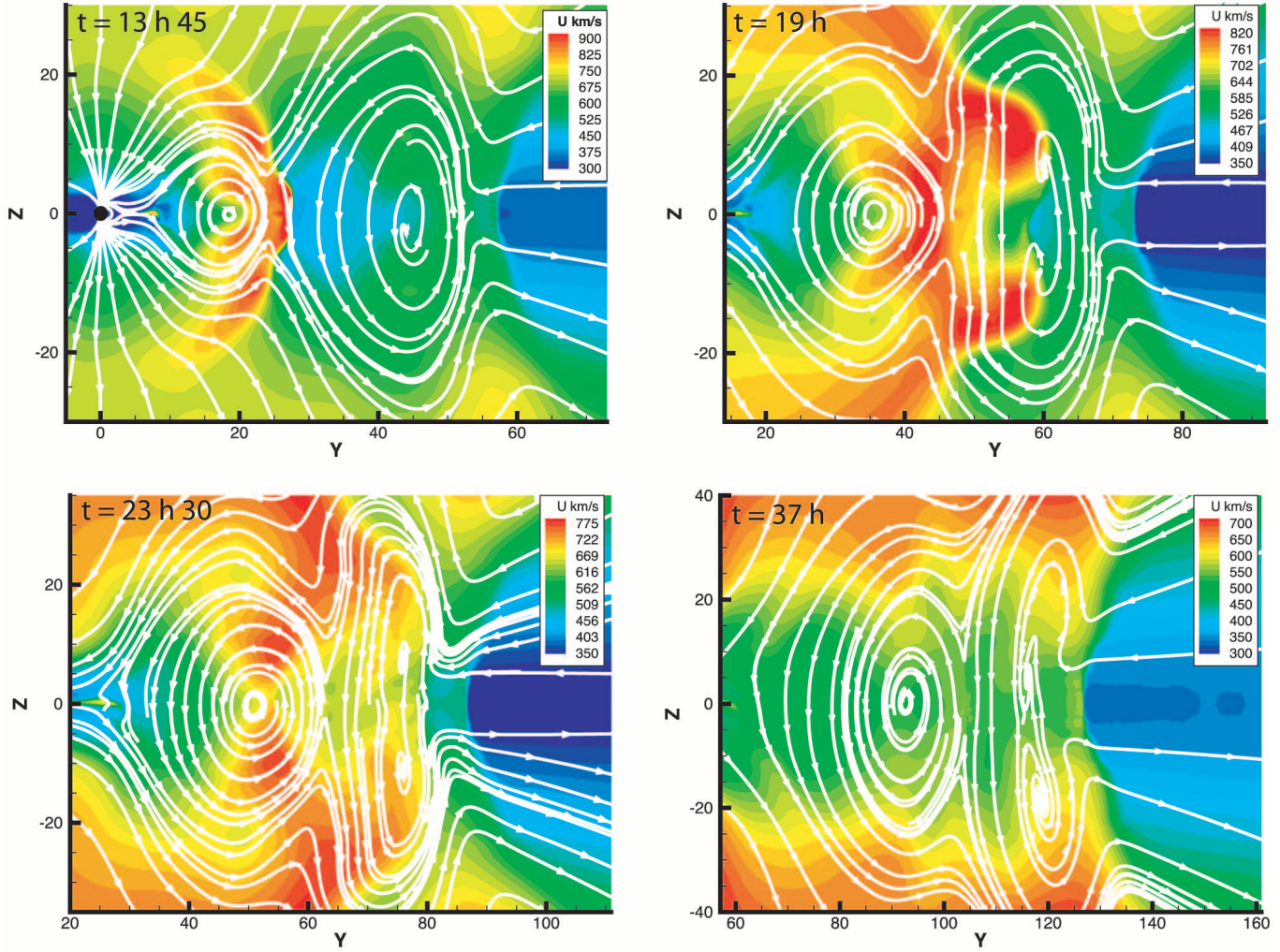


FIG. 6.—Plasma speed in the y - z plane at four different times during the interaction of the two CMEs. “Streamlines” drawn in white illustrate the direction of the magnetic field in the plane. *Top left*: $t = 13.75$ hr, as the trailing shock enters the first cloud. *Top right*: $t = 19$ hr, as the trailing shock has just passed the center of the first cloud. *Bottom left*: $t = 23.5$ hr, as the trailing shock enters the dense sheath of plasma associated with the leading shock. *Bottom right*: $t = 37$ hr; note the uniformization of the speed in the two clouds at this time. Also note the change in scales between the different panels.

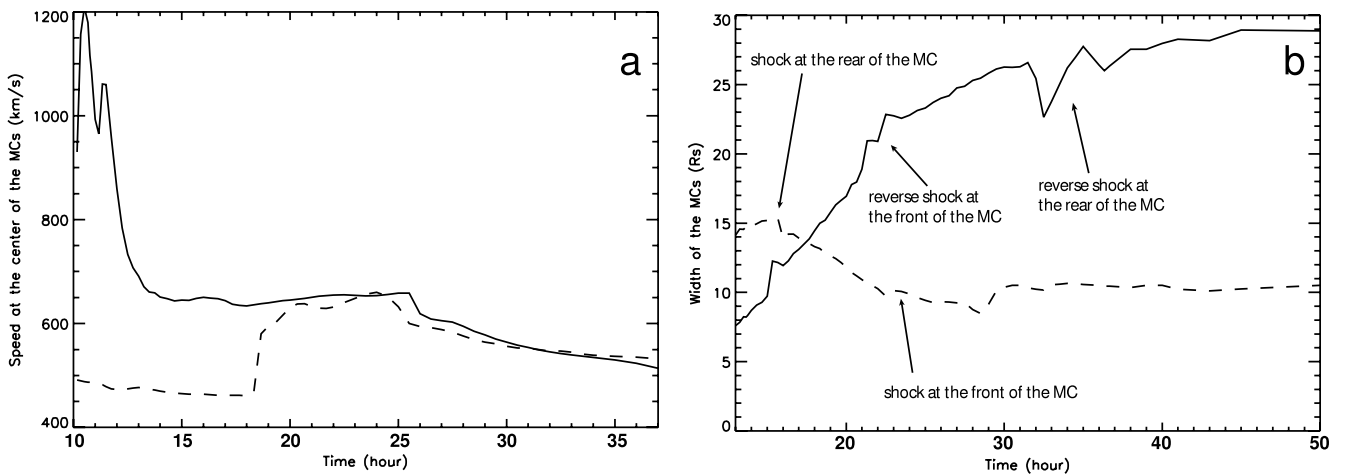


FIG. 7.—(a) Plasma speed at the center of the two clouds. (b) Radial width of the two clouds. *Dashed line*: First cloud. *Solid line*: Second cloud. The second CME is initiated at time $t = 10$ hr.

Later, the speed at the center of the flux rope decreases as the cloud is expanding and the magnetic field is reorganizing itself. The time evolution of the speed at the center of the first cloud is shown as a dashed line in Figure 7a. A simple second-order polynomial fit to the time-height series of the center of the first flux rope between 0 and 37 hr gives an average speed of 600 km s^{-1} and an acceleration of 0.19 m/s^2 .

We can compare the arrival time at Earth of this flux rope with the one in Manchester et al. (2004b), since the exact same parameters are used in both cases to generate the CME. We find that the first cloud arrives at 1 AU ($x = 0 R_\odot$, $y = 215 R_\odot$, $z = 20 R_\odot$) approximately 71 hr after the launch of the first CME, whereas in the case without interaction, the cloud arrives at Earth 77 hr after the initiation of the CME.

Another way to quantify the effect of the shock on the first MC is to study its radial width (in the y -direction). We calculate the width as the distance between the two extrema of B_z in the x - y plane along the $\{x = 0\}$ line. Up to time $t = 16$ hr, the width of the first cloud slowly increases, due to the expansion of the cloud. At time $t = 16$ hr, the shock reaches the minimum of B_z . Since the rear edge of the cloud is now in the downstream region associated with the shock, whereas the front edge is in the upstream region, the rear edge is traveling at a faster speed than the front edge. Thus, the width of the first cloud decreases and the cloud continues its contraction until time $t = 22.5$ hr. After the shock goes through the front part of the cloud, the whole cloud is in the downstream region associated with the trailing shock and travels at an almost uniform speed. The width of the first cloud remains approximately constant but at a value about 33% less than its width before the shock-cloud interaction. This is due to the contraction of the cloud during the 6 hr when the different parts of the cloud are traveling at different speeds. The evolution of the width of the first cloud is shown as a dashed line in Figure 7b.

5.2. Reconnection and Reverse Shock Associated With the Collision of the Two Clouds

By the time the two clouds collide, the trailing shock is propagating inside the first cloud. Thus, the back part of the first cloud is in the downstream region of the trailing shock and it has an increased speed compared to the rest of the cloud. Reconnection between the two clouds occurs at a slow rate in a region of about $2\text{--}3 R_\odot$ wide near the equatorial current sheet. The back of this reconnection region is traveling with a speed comparable to that of the front edge of the second cloud, whereas its front part is traveling with a speed comparable to that of the rear edge of the first MC. Both speeds are at first almost identical. As the trailing shock moves away from the back of the first magnetic cloud, the speed of the rear edge of this cloud slowly decreases. Therefore, the reconnection region continues to be pushed by the fast stream of the second cloud, while it is prevented to travel at this speed by the slower first cloud. Moreover, the reconnection leads to a reduced magnetic field strength and Alfvénic speed in this region. At time $t = 17$ hr, the difference in speed between the back and the front parts of the reconnection region becomes greater than the local Alfvénic speed (around 90 km s^{-1}). This results in the formation of a reverse fast-mode shock, whose effect is to reduce the speed in the back of the reconnection region and in the front edge of the second MC. Associated with this reduction in speed, there is an increase in density, magnetic field (fast-mode shock), and temperature. At time $t = 19$ hr, after the reverse shock's passage in the reconnection region, the region has an almost uniform speed. At later times, as the reverse shock travels into the higher density material of the second MC, it

decelerates and loses strength and effectiveness. It eventually disappears as it reaches the interface between the second MC and the solar wind (around time $t = 42$ hr). We propose a possible candidate for one of these reverse shocks in the data analyzed by Farrugia & Berdichevsky (2004) in the 1979 April 2–6 storm, at time 9.5 hr, April 6, associated with the interaction between the third and fourth ejecta.

5.3. Evolution of the Second Magnetic Cloud

We track the position of the center of the second flux rope, defined as the position at which $B_z = 0$. A second-order polynomial fit of the time-height sequence of the center of this cloud gives an average speed of 740 km s^{-1} and a deceleration of -0.996 m s^{-2} , about 5 times larger than the acceleration of the first cloud. This result is in good agreement with the conclusion by Farrugia & Berdichevsky (2004) that the deceleration of the trailing cloud is greater than the acceleration of the leading cloud. However, this difference, in our case, can be partly explained by the acceleration of the first cloud by the trailing shock and the deceleration of the faster second CME due to the collision of the two clouds, instead of being explained by a relative difference in the masses of the ejecta. Analyzing the speed at the center of each cloud as plotted in Figure 7a leads to a more complex picture than the uniform acceleration/deceleration from the time-height plots. In fact, most of the acceleration of the first cloud is associated with the passage of the trailing shock at the cloud center at time $t = 18.3$ hr. Before this time and after $t = 25.5$ hr, the first cloud is decelerating due to its expansion. The speed at the center of the second cloud is almost constant from time $t = 14$ to 25.5 hr. The steep deceleration at this time is due to the passage of the reverse shock, and after that, the cloud is freely expanding (thus decelerating).

We also track the width of the second MC as described in § 5.2. The result is shown as a solid line in Figure 7b. Before any interaction occurs (before time $t = 15$ hr), the second cloud is expanding at a faster rate than the first cloud. This is due to the fact that the second cloud has been propagating for 10 hr less and that it encounters less dense material. At time $t = 15.3$ hr, the front edge of the second cloud shows what appears as an acceleration. This is actually not associated with any acceleration of the plasma at the front edge of the MC but with a reorganization of the spatial distribution of the magnetic field in the flux rope, probably due to the beginning of the reconnection between the clouds.

The reverse shock leads, at first, to a reorganization of the magnetic field near the front edge of the cloud, and is associated with a faster expansion of the cloud. Later, since the reverse shock leads to a deceleration of the plasma in the downstream region, the front edge travels slower and the expansion rate of the cloud is reduced. When the reverse shock is near an extremum of B_z , the width of the clouds is hard to compute, since then, the extremum of B_z is traveling with the reverse shock. This leads to a complex picture around time $t = 22$ and 32 hr.

6. PROPERTIES OF THE CMEs AT 1 AU

At 1 AU, the two flux ropes have evolved to show characteristics commonly associated with multiple MCs, namely two high magnetic field strength regions separated by a region of increased β and temperature, smooth variation of the magnetic field in each cloud, compressed and heated first cloud, low proton density in both clouds and an uniform speed profile. Figure 8 shows on the left side a three-dimensional isosurface of magnetic field strength ($|B| = 20 \text{ nT}$) as the shock reaches 1 AU, showing

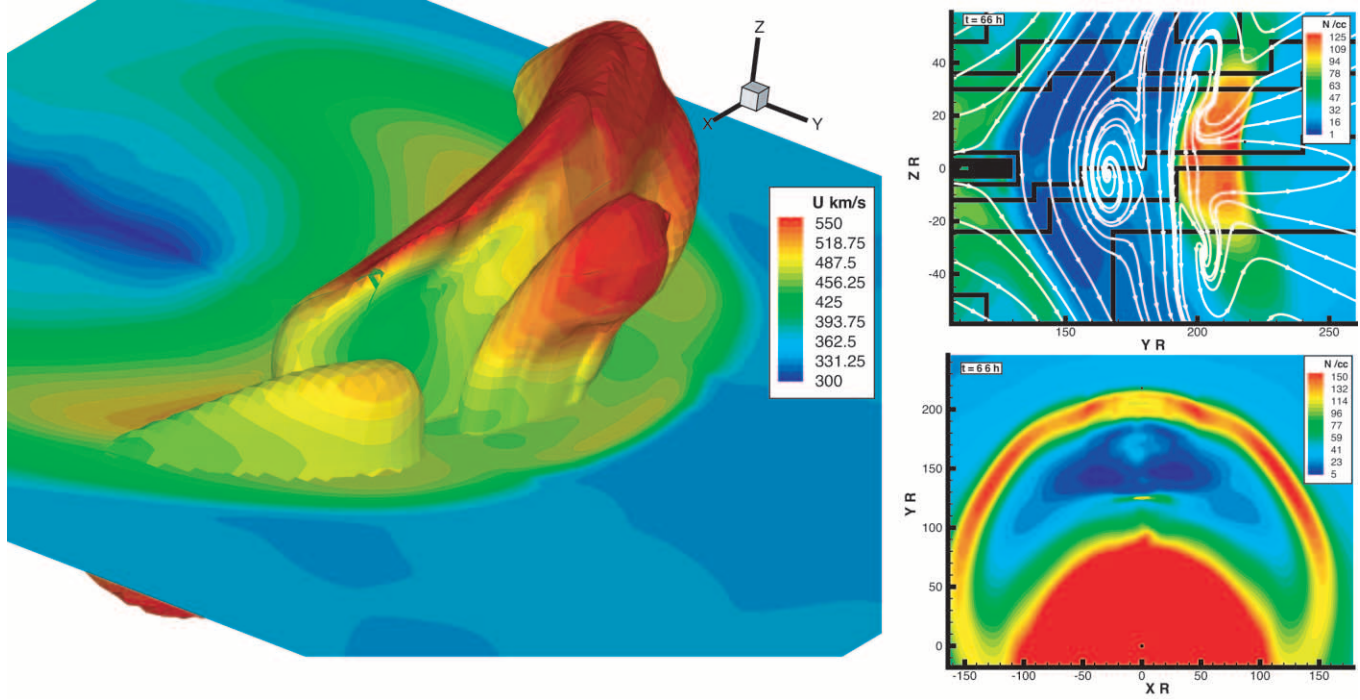


FIG. 8.—Left: Three-dimensional representation of the CME 66 hr after the initiation of the first CME. A three-dimensional isosurface of magnetic field strength is drawn where $|B| = 20$ nT. The color code shows the plasma velocity in the x - y plane and on the isosurface. Right: Two frames showing the number density of the CMEs, 66 hr after the initiation of the first CME, when the shock reaches 1 AU. The top panel shows the number density in the y - z plane, with the streamlines representing magnetic field lines, the black lines the boundary of the mesh, and the black dot the position at which the data at 1 AU are taken ($x = 0 R_\odot$, $y = 218 R_\odot$, $z = 10 R_\odot$). The bottom panel shows the number density in the x - y plane, with the small black dot representing the position at which the data at 1 AU are taken and the slightly larger black dot at the bottom of the panel representing the Sun.

the two MCs, with a first compressed cloud, and an over-expanded second cloud. The right side of this picture shows two-dimensional cuts in the y - z (top) and x - y (bottom) planes representing the number density of the CMEs at the same time. Analyzing those pictures, we see the extreme compression of the first flux rope, whose front part appears to have entered the high-density region following the front shock, the large extent of this dense sheath of plasma (with number density over 90 cm^{-3} for almost $20 R_\odot$ in the y -direction) and the uniform speed (around 480 km s^{-1}) of the two flux ropes in the equatorial plane. The front shock has a very large lateral (in the x - y plane) extent and is weakest in the Sun-Earth line direction. The two flux ropes cannot be distinguished in this lateral plane based on the density structure, but the low-density cavity associated with the second MC has a lateral extent (in the x -direction) of more than $150 R_\odot$.

More information can be obtained by analyzing the results of the simulation at 1 AU as seen in Figure 9. The shock reaches 1 AU ($x = 0 R_\odot$, $y = 218 R_\odot$, $z = 10 R_\odot$) by time $t = 66$ hr. As the shock passes 1 AU, the density increases by a factor of 3.567 and the velocity jumps from 342 to 486.8 km s^{-1} . The density first decreases behind the shock, but then increases again before the contact discontinuity at the surface of the flux rope. This increase in density in the rear part of the sheath of plasma is specific to this model of CME interaction, and was not found in Manchester et al. (2004b). At the contact discontinuity, separating the dense sheath and the first MC, the density drops by a factor of 9 to about 11 cm^{-3} and remains nearly constant in the first flux rope. In the reconnection region between the two clouds, the density increases to about 15 cm^{-3} and decreases as the second cloud reaches Earth to a minimum value of 1.5 cm^{-3} . Temperature increases from 6.8×10^4 to 1.07×10^6 K behind the shock. Contrary to the case of one flux rope, here the maximum temperature is

reached at the shock and not inside the flux rope. This temperature jump at the shock is a factor of 2.5 larger than the one found for the “undisturbed” case (Manchester et al. 2004b). Since the density and velocity jumps are found to be similar between those two simulations (the interaction case being about 10% larger), the temperature is the only clear indicator that the shock observed at Earth is the result of the merging of two shocks. The minimum and maximum temperatures in the first flux rope are, respectively, 4.07×10^5 and 6.8×10^5 K. The region between the two clouds is highly heated by the reconnection between the flux ropes, and we find a maximum temperature of 1.11×10^6 K. The second cloud is colder than the first one, with a minimum and maximum temperature of 3.5×10^4 and 2.25×10^5 K, respectively.

At the shock, the magnetic field jumps from 1.52 to 4.01 nT. The maximum magnetic field strength of 26 nT is obtained in the first cloud 11 hr after the shock’s passage and is just slightly larger (by 1 nT) than the one found by Manchester et al. (2004b). The magnetic field in the reconnection region reaches a minimum value of 5.4 nT. The second cloud has a maximum magnetic field strength of 21.5 nT. As the first flux rope passes 1 AU, B_z turns northward for about 7 hr reaching a maximum value of 6.85 nT (20 nT in the no-interaction case). All the northward magnetic field of the first cloud appears to be in the rear part of the dense sheath of plasma, probably due to the compression of the first cloud. The northward part of the first cloud ends with what appears to be the result of the interaction of the trailing shock with the contact discontinuity (shown by the third vertical dashed line on the right column of Fig. 9), with a large decrease in the number density, and a faster increase in the magnetic field strength. The magnetic field then smoothly rotates southward to reach a maximum value of -24.65 nT (-20 nT in the no-interaction case).

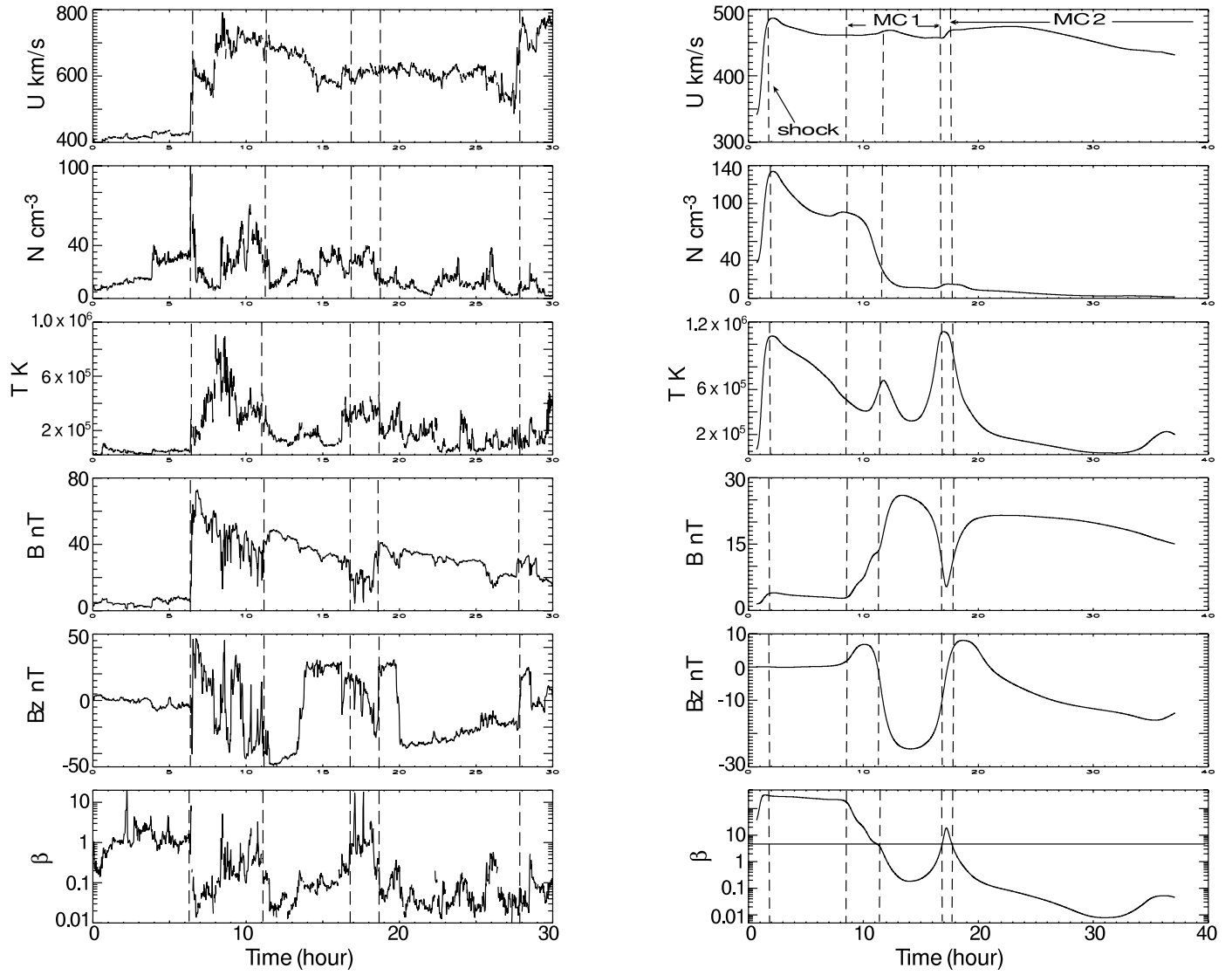


FIG. 9.—Plasma properties near 1 AU ($x = 0 R_{\odot}$, $y = 218 R_{\odot}$, $z = 10 R_{\odot}$) as function of time, showing (from top to bottom) proton speed, number density, temperature, magnetic field strength, B_z , and plasma β . The numerical model is on the right column; the left column shows *ACE* data for the period 2001 March 30 (18 hr)–April 1 adapted from Wang et al. (2003a). On the left column, the vertical lines represent (from left to right) the shock's arrival, the beginning of the first cloud, the end of the first cloud, the beginning of the second cloud, and the end of the second cloud (fast ejecta reach Earth at this time). On the right column, the vertical lines represent (from left to right) the shock's arrival, the beginning of the first cloud, the possible contact discontinuity, the end of the first cloud, and the beginning of the second cloud.

The magnetic field remains southward for about 6 hr in the first cloud. The reconnection region corresponds to $B_z \sim 0$ nT. As the second flux rope passes 1 AU, the magnetic field becomes northward again for about 3.6 hr, reaching a maximum value of 8 nT, and then rotates southward for almost a day, reaching a maximum value of -16 nT. This additional southward IMF is due to the reconnecting sheath of magnetic field behind the second flux rope as described in Manchester et al. (2004b). The reconnection region is associated with values of β above unity, corresponding to the low magnetic field and high proton temperature. Such high- β interaction regions are described by Wang et al. (2003a) for three different multiple-MC events in 2001 March–April.

At Earth, the global structure composed by the two MCs is about $50 R_{\odot}$ wide (between the maximum northward B_z of the first cloud and the maximum southward B_z of the second cloud) and the second MC accounts for about 80% of this width ($40.6 R_{\odot}$). The structure of the complex ejecta is a highly compressed MC followed, 2.5 R_{\odot} later, by an overexpanded MC.

This structure is very different from the simple superposition of two identical MCs, and one can expect a modification of the geo-effectiveness of the event.

Making a comparison between the model and *ACE* data, we find that the model is in good qualitative agreement with the data, even though it gives a much more simplified picture. The two clouds are preceded by a very strong shock with density over 100 cm^{-3} and speed over 700 km s^{-1} behind the shock. The speed profile is not uniform in the two clouds, but the rear end of the first cloud and the second cloud have very similar speeds. The two clouds are separated by a region about $8.5 R_{\odot}$ wide (based on the criterion $\beta > 0.1$) with an large β ($\beta_{\max} > 18$), large temperature ($T_{\max} > 4.5 \times 10^5 \text{ K}$), and low magnetic field strength ($B_{\min} < 11.5 \text{ nT}$ to be compared with values in the clouds around 30 nT). The two clouds in the events of March 31, 2001 were 9.5 and $18 R_{\odot}$ wide with a maximum southward B_z of -47.9 nT (in the first cloud). It lead to a peak value of Dst of -387 nT (Wang et al. 2003a). Another event described by Wang et al. (2003a) is the 2001 April 11–13 storm with the two

clouds being 6.35 and $35.2 R_{\odot}$ wide, with a maximum southward B_z of -34 nT (in the first cloud) and leading to a peak value of Dst of -271 nT.

7. DISCUSSION AND CONCLUSIONS

We have investigated the complex interaction of two coronal mass ejections (CMEs) propagating in the same direction from Sun to Earth. We find that the trailing shock plays the key role to generate the structure of the multiple magnetic clouds (MCs) at 1 AU. In our simulation, the propagation of the trailing shock in the first cloud is indeed essential to homogenize the speed of the two clouds. Since the shocked first cloud is still slower than the second one, a reverse shock propagates backward in the second cloud to decrease its speed. In effect, the final speed of the two ejecta is comparable but slightly lower than the speed of the second (faster) cloud. The uniformization of the speed of the two MCs associated with the trailing and reverse shocks explains why, at Earth, complex ejecta resulting from interacting CMEs appear to have an uniform speed (Burlaga et al. 2002; Farrugia & Berdichevsky 2004)

Wang et al. (2005) consider the collision of two clouds without simulating their associated shock. They find that the final speed of the multiple MCs is the one of the first (slower) cloud. Comparing the transit time to the initial speeds of the ejecta should help distinguishing between these two hypotheses. Manoharan et al. (2004) conclude in their statistical studies of interplanetary shock propagation and interacting CMEs that CME interaction tends to slow down the CME and its associated shock. However, event studies such as the one of Farrugia & Berdichevsky (2004) tend to show that the transit time of complex ejecta or multiple MCs is reduced compared to the expected transit time based on the initial speeds of the ejecta.

Another hypothesis to explain the final higher speed of the multiple MCs is that an elastic collision between the clouds is associated with momentum transfer from the faster cloud to the slower cloud (Farrugia & Berdichevsky 2004). In this case, the authors propose that the trailing shock disappears in the first

cloud as its speed relative to the ejecta becomes sub-Alfvénic. However, the strengthening of the leading shock that they also report, appears to be best explained by a shocks' merging process. All three of these hypotheses (inelastic collision, elastic collision, and trailing shock–first cloud interaction) may happen for different types of CMEs depending on their speed relative to the solar wind (presence or absence of CME-driven shocks) and on the magnetic field strength in the first cloud. Our study reflects the case of two fast CMEs with the second shock remaining faster than the local magnetosonic speed at all times. In this case, the compression and heating of the first cloud are mainly due to the passage of the trailing shock in the cloud. The leading shock's strengthening is due to the shocks' merging and is associated with a contact discontinuity between the “old” and “new” downstream regions. The main difference between this result and the work of Poedts et al. (2002), which states that the shocks' merging is associated with the creation of a rarefaction wave, is that, in our case, the pressure is quickly dropping behind the overtaking shock, and a continuous-pressure interface (contact discontinuity) is able to match the “old” and “new” downstream regions.

The compression of the magnetic field in the first cloud, and the large duration of a strong southward B_z may lead to an increased geoeffectiveness, as it is the case for the multiple-MC event described in this paper.

We would like to thank Kenneth Powell and Paul Drake for useful comments and discussions on the nature of the reverse shock and the shock-shock merging. We would also like to thank Ilia Roussev for useful comments and discussions on the simulation. The simulations reported here were carried out on an Origin3800 supercomputer at NASA Ames. The research for this manuscript was supported by Department of Defense MURI grant F49620-01-1-0359, NSF CISE grant ACI-9876943, NSF ITR grant 0325332, and NASA AISRP grant NAG5-9406 at the University of Michigan. We would also like to thank NSF for a travel grant for the SHINE 2005 meeting.

REFERENCES

- Burlaga, L. F., Plunkett, S. P., & St. Cyr, O. C. 2002, *J. Geophys. Res.*, 107, 1
- Burlaga, L. F., Sittler, E., Mariani, F., & Schwenn, R. 1981, *J. Geophys. Res.*, 86, 6673
- Cargill, P. J. 1990, *Phys. Fluids B*, 2, 10, 2294
- Farrugia, C., & Berdichevsky, D. 2004, *Ann. Geophys.*, 22, 3679
- Gibson, S., & Low, B. C. 1998, *ApJ*, 493, 460 (GL98)
- Gopalswamy, N., Yashiro, S., Kaiser, M. L., & Howard, R. A. 2003, *Adv. Space Res.*, 32, 2613
- Gopalswamy, N., Yashiro, S., Michalek, G., Kaiser, M. L., Howard, R. A., Reames, D. V., Leske, R., & von Rosenvinge, T. 2002, *ApJ*, 572, L103
- Groth, C. P. T., DeZeeuw, D. L., Gombosi, T. I., & Powell, K. G. 2000, *J. Geophys. Res.*, 105, 25053
- Hundhausen, A. J. 1993, *J. Geophys. Res.*, 98, 13177
- Lugaz, N., Manchester, W. B., IV, & Gombosi, T. I. 2005, *ApJ*, 627, 1019
- Manchester, W. B., IV, Gombosi, T. I., Roussev, I., DeZeeuw, D. L., Sokolov, I. V., Powell, K. G., Tóth, G., & Opher, M. 2004a, *J. Geophys. Res.*, 109, 1102
- Manchester, W. B., IV, Gombosi, T. I., Roussev, I., Ridley, A. J., DeZeeuw, D. L., Sokolov, I. V., Powell, K. G., & Tóth, G. 2004b, *J. Geophys. Res.*, 109, 2107
- Manchester, W. B., IV, et al. 2005, *ApJ*, 622, 1225
- Manoharan, P. K., Gopalswamy, N., Yashiro, S., Lara, A., Michalek, G., & Howard, R. A. 2004, *J. Geophys. Res.*, 109, 6109
- Nitta, N. V., & Hudson, H. S. 2001, *Geophys. Res. Lett.*, 28, 3801
- Odstrcil, D., Linker, J. A., Lionello, R., Mikić, Z., Riley, P., Pizzo, V. J., & Luhmann, J. G. 2002, *J. Geophys. Res.*, 107, 14
- Odstrcil, D., Vandas, M., Pizzo, V. J., & MacNeice, P. 2003, in *AIP Conf. Proc.* 679, *Solar Wind 10*, ed. M. Velli, R. Bruno, & F. Malara (Melville: AIP), 699
- Parker, E. N. 1963, *Interplanetary Dynamical Processes* (New York: Wiley)
- Pneuman, G. W., & Kopp, R. A. 1971, *Sol. Phys.*, 18, 258
- Poedts, S., van der Holst, B., de Sterck, H., van Driel-Gesztelyi, L., Csík, Á., Milesi, A., & Deconinck, H. 2002, in *Proc. Second Solar Cycle and Space Weather Euroconference*, ed. H. Sawaya-Lacoste (ESA SP-477; Noordwijk: ESA), 263
- Powell, K. G., Roe, P. L., Linde, T. J., Gombosi, T. I., & de Zeeuw, D. L. 1999, *J. Comput. Phys.*, 154, 284
- Riley, P., Linker, J. A., Mikić, Z., Odstrcil, D., Pizzo, V. J., & Webb, D. F. 2002, *ApJ*, 578, 972
- Sokolov, I. V., Roussev, I. I., Gombosi, T. I., Lee, M. A., Kóta, J., Forbes, T. G., Manchester, W. B., & Sakai, J. I. 2004, *ApJ*, 616, L171
- Usmanov, A. V., & Dryer, M. 1995, *Sol. Phys.*, 159, 347
- Vandas, M., Fischer, S., Dryer, M., Smith, Z., Detman, T., & Geranios, A. 1997, *J. Geophys. Res.*, 102, 22,295
- Vandas, M., & Odstrcil, D. 2004, *A&A*, 415, 755
- Wang, Y. M., Wang, S., & Ye, P. Z. 2002, *Sol. Phys.*, 211, 333
- Wang, Y. M., Ye, P. Z., & Wang, S. 2003a, *J. Geophys. Res.*, 108, 6
- Wang, Y. M., Ye, P. Z., Wang, S., & Xue, X. H. 2003b, *Geophys. Res. Lett.*, 30, 33
- Wang, Y., Zheng, H., Wang, S., & Ye, P. 2005, *A&A*, 434, 309
- Webb, D. F., Howard, R. A., & Jackson, B. V. 1996, in *AIP Conf. Proc.* 382, *Solar Wind 8*, ed. D. Winterhalter et al. (Melville: AIP), 97
- Wu, S. T., Guo, W. P., Michels, D. J., & Burlaga, L. F. 1999, *J. Geophys. Res.*, 104, 14789